PCCP

PAPER
Erbe *et al.*
A mechanistic study of the electrochemical oxygen reduction on the
model semiconductor n-Ge(100) by ATR-IR and DFT

PCCP

A mechanistic study of the electrochemical oxygen reduction on the model semiconductor n-Ge(100) by ATR-IR and DFT†

Simantini Nayak, P. Ulrich Biedermann, Martin Stratmann and Andreas Erbe*

The electrochemical oxygen reduction reaction (ORR) on a n-Ge(100) surface in 0.1 M $HClO_4$ was investigated *in situ* and operando using a combination of attenuated total reflection infrared (ATR-IR) spectroscopy and density functional (DFT) calculations. The vibrational modes of the detected intermediates were assigned based on DFT calculations of solvated model clusters such as Ge-bound superoxides and peroxides. ATR-IR shows the Ge-bound superoxide with a transition dipole moment oriented at $(28 \pm 10)°$ with respect to the surface normal. At slightly negative potentials, the surface-bound peroxide is identified by an OOH bending mode as a further intermediate, oriented at a similar angle. At strongly negative potentials, a surface-bound perchlorate is found. The findings indicate a multistep mechanism of the ORR. The reaction is furthermore coupled with the hydrogen evolution reaction (HER).

1 Introduction

The electrochemical oxygen reduction reaction (ORR) is a crucial reaction for a number of fields in chemistry, including conversion of chemical to electrical energy, and corrosion.[1,2] The lack of understanding of the reaction mechanism of the electrochemical ORR is a major bottleneck in the development of efficient fuel cells and in the prevention of corrosion. The ORR involves the transfer of 4 electrons and 4 protons to the O_2 molecule and breaking of the formal double bond. The net reaction is $O_2 + 4e^- + 4H^+ \rightarrow 2H_2O$ in acidic solution.[1,2] Recently, interest in the reaction mechanism has increased due to its role in fuel cells and batteries.[3–7] Many studies have been performed to find ORR catalysts with increased performance or lower cost than existing noble metal catalysts, and to understand the reaction mechanism.[8–11] Several major pathways have been put forward, a direct mechanism based on dissociative adsorption of O_2 on an electrode surface, or different variants of multistep reaction mechanisms with step-by-step electron transfer, which proceed *via* the superoxide radical anions and/or peroxides, to the final dissociation of the O–O bond.[1,2,7,12–16] A general scheme of possible intermediates has been constructed.[12,17–19]

Traditionally, intermediates that are stable enough to diffuse away from the electrode surface have been detected by electrochemical experiments.[12,20] Furthermore, vibrational spectroscopic techniques have been used to detect intermediates during ORR on rough noble metal films relevant to fuel cell applications.[21–29] Vibrational spectroscopy is a powerful tool to analyze the nature of transient oxygen-related species on the surface, as peak frequencies can clearly distinguish between double bonds (~ 1550 cm^{-1}) as present in O_2, single bonds (~ 800 cm^{-1}) as present in peroxides including H_2O_2, and bonds with bond order 1.5 (~ 1200 cm^{-1}) present in superoxides.[22,30] A detailed literature overview of the assignment of vibrational frequencies of reported intermediates, and selected data for reference compounds, is given in the ESI.† Experimental studies have been complemented by computational studies, which lead to more detailed insight into adsorption sites, relative stabilities and the nature and orientation of the species.[23,31,32] Detailed experimental studies including the orientation of intermediates have been reported for flat solid/gas interfaces,[33,34] but are so far lacking under conditions of electrochemical reactions.

The crystalline semiconductor Ge has been proposed as a model for semiconducting passive films,[35] as under ambient conditions most metallic materials are covered with protective semiconducting oxides.[36] More recently, semiconductors and other non-metallic materials have been suggested as a replacement of precious metals in electrocatalysis.[5,6,37]

Ge exhibits a potential-dependent transition from a hydroxide covered to hydrogen terminated surface. This transition has

Max-Planck-Institut für Eisenforschung GmbH, Max-Planck-Str. 1, 40237, Düsseldorf, Germany. E-mail: a.erbe@mpie.de, aerbe@arcor.de; Fax: +49 211 6792 218; Tel: +49 211 6792 890

This journal is © the Owner Societies 2013

Phys. Chem. Chem. Phys., 2013, **15**, 5771–5781 | **5771**

originally been inferred from electrochemical experiments[38] and was later confirmed using attenuated total reflection infra-red (ATR-IR) spectroscopy and quartz-crystal microbalance experiments.[39–41] Without systematic studies of the ORR on Ge, this transition has been proposed to be related to the onset of the ORR, as it involves a radical surface state.[40,42,43]

In this work, ATR-IR spectroscopy and density functional theory (DFT) calculations have been used to study the mechanism of the ORR on Ge(100) in 0.1 M HClO$_4$.

2 Materials and methods

2.1 Electrochemical and spectroscopic experiments

The setup consists of the optical base of the horizontal ATR unit SpectraTech Model 0001-100 (SpectraTech, Stamford, CT). The crystal plate was removed from the unit, and replaced by a copper piece that is used to contact the Ge ATR crystals. It was fixed on a PTFE mount to prevent electric contact with the optical base. Trapezoidal Sb-doped n-type Ge(100) crystals (Crystaltechno, Moscow, Russia) were used as substrates. The crystals have a specified resistivity of 10–40 Ω cm and a size of 52 mm × 20 mm × 0.5 mm. The short edges were polished to an angle of 30°, leading to an angle of incidence of 60° at the Ge/electrolyte interface. The Ge crystal was placed in a groove on the copper piece and moved along the direction of the beam until maximum transmitted intensity through the whole system was observed. A PTFE basin was used to hold the electrolyte with a FPM O-Ring in direct contact with the Ge crystal. After alignment of the IR light path, the PTFE basin was screwed onto the base part, pressing the back of the Ge crystal against the copper surface and sealing the electrochemical cell. The cell was covered with a Teflon lid which contains bores as gas inlet and outlet, and connections for the reference electrode (RE) and counter electrode (CE).

Several published cleaning protocols have been tried for the Ge(100) surface.[40,43,44] Most of them lead to surface roughening. Therefore, the crystals were cleaned by immersing them in neutral Extran lab detergent (VWR) for 1 h. Immersion was followed by rinsing with ultrapure water several times, and leaving them in 2-propanol for 1 h. The crystals were subsequently rinsed with excessive amounts of deionised ultrapure water and dried under an N$_2$ stream prior to experiments. The final cleaning was performed by electrochemical oxidation of the species inside the spectroelectrochemical cell prior to experiments. Eight cycles of scans in an anodic direction from +0.21 to −0.79 (all electrode potentials are given with respect to the standard H$_2$ electrode, SHE) were performed. The resulting final cyclic voltammograms (CVs) were in good agreement with references.[38–40,43] The absence of C–H stretching modes in the subsequent experiments is an additional indication for the successful cleaning of the Ge surface.

In the geometry used, the Ge crystal acted as a working electrode (WE) with an electrode area of 5.5 cm^2. The dimensions of the crystal imply that there are ∼100 internal reflections probing the WE/electrolyte interface. A double junction Ag/AgCl/ 3 M KCl microreference electrode (MI-403, MICROELECTRODES,

INC., Bedford, NH, USA) was used as a RE. A Pt loop (99.99%, 0.4 mm diameter and 0.2 m length), (Goodfellow, Huntingdon, UK) was used as a CE. 0.1 M HClO$_4$ (70%, Sigma-Aldrich) was used as an electrolyte. The electrolyte was saturated with O$_2$ or Ar, respectively, by purging the solution with gas prior to the experiment. During experiments, the gas volume above the electrolyte was continuously purged with the respective gas. All experiments were carried out at ambient temperature of (23 ± 2) °C.

IR spectra were recorded on a FTS 3000 Fourier transform IR spectrometer (Biorad, Palo Alto, CA, USA; now part of Agilent Technologies) using a mercury cadmium telluride (MCT) detector. IR spectra were recorded in s- and p-polarisation co-adding 1000 scans with a spectral resolution of 4 cm^{-1}. IR spectra are displayed as absorbance defined as

$$A = -\log_{10}\left(\frac{I_s}{I_o}\right) \qquad (1)$$

where I_s and I_o represent the light intensity of the sample- and reference-spectrum, respectively. All the spectra were referred against the initial potential (+0.01 V$_{SHE}$ unless stated otherwise). Spectroelectrochemical experiments were carried out in potential steps of 100 mV under potentiostatic conditions, with a simultaneous recording of currents in chronoamperometry mode, and IR spectra. An Iviumstat potentiostat (Ivium, Eindhoven, The Netherlands) was used to measure all the electrochemical data.

For spectra recorded in an Ar saturated electrolyte, the residual absorbance from bulk ClO$_4^-$ was subtracted from the spectra by subtracting a spectrum such as that shown in Fig. S3 (ESI†) from the measured spectra using the algorithm implemented in the program specsubtr.[45] Using this procedure, only spectral components visible in the bulk are removed from the spectra. Such spectral components may show up in the resulting difference spectra, e.g. because of changes in the wetted working electrode area in the order of ∼μm^2. In particular, no components generated during the electrochemical treatment are removed by the subtraction procedure.

For isotope exchange experiments, a slightly modified setup was used, where the electrolyte was saturated outside the ATR-IR cell initially with Ar, which was later replaced by ^{18}O$_2$, and then pumped into the spectroelectrochemical cell.

2.2 Quantification of spectra and electric fields at interfaces

2.2.1 Calculation of orientation. The dichroic ratio $D = A_p/A_s$ (A_p – integrated absorbance of respective band in p-polarisation, A_s – integrated absorbance of respective band in s-polarisation) was used to determine the orientation of the transition dipole moment (TDM) of different species with respect to the surface normal. The orientational order parameter S_2 has been determined from the experimental D using $D = \frac{I_{0x}}{I_{0y}} + \frac{I_{0z}}{I_{0y}}\left(1 + \frac{3S_2}{1 - S_2}\right)$.[46] The squared amplitudes of the electric field components at the interface I_{0x}, I_{0y} and I_{0z} are calculated from the parameters of the experimental system.[46,47] The right-handed Cartesian coordinate system is used where the ATR internal reflection element's surface normal points to the z direction, and the x direction is the projection of the

5772 | Phys. Chem. Chem. Phys., 2013, 15, 5771–5781

This journal is © the Owner Societies 2013

direction of propagation onto the internal reflection element's surface.[46]

S_2 is related to the angle θ between TDM and surface normal as $S_2 = \dfrac{3\langle\cos^2(\theta)\rangle - 1}{2}$.[46] In all cases, only a single orientation has been assumed in the orientation distribution function of each TDM. A random orientation resulting in the ''magic angle'' of 54.6° is expected for dissolved or weakly physisorbed species.[46]

It should be noted that in the case of coexistence of a certain (small) concentration of dissolved isotropically oriented species with the oriented species, an even more upright orientation of the surface-bound intermediate would be required to arrive at the observed polarization dependence. It should also be pointed out that the averaging of the tilt angle is over $\cos^2(\theta)$.[46] Detailed discussions including examples of orientation distribution can be found elsewhere.[46,48,49]

2.2.2 Calculation of A_{iso}. Because of the effect of orientation, in ATR-IR spectroscopy, the surface concentration is not directly proportional to the absorbance integrated over a certain absorption band, as in the case of spectroscopy in transmission geometry. Therefore, for each of the major observed absorption bands, a quantity A_{iso} has been derived from A_s and A_p, which is proportional to the isotropic absorbance, and hence to the surface concentration.[50] This quantity is given as

$$A_{iso} = A_s\left(2 - \frac{I_{0x}}{I_{0z}}\right) + A_p\frac{I_{0y}}{I_{0z}}. \qquad (2)$$

In the course of this work, only the A_{iso} of the most intense absorption peak observed during the ORR is reported. Therefore, no further index is used to describe the association to an absorption peak.

2.3 Density functional theory calculations

DFT calculations were done using the program package TURBOMOLE Version 6.2.[51] The hybrid density functional B3-LYP[52–54] was used with the basis set def2-TZVP,[55,56] and the RI-JK approximation.[57] The structures have been optimized using redundant internal coordinates until the energy changes are below 10^{-7} Hartree and forces are below 10^{-4} Hartree Bohr^{-1} in calculations without the continuum solvation model. In geometry optimizations with the continuum solvation model the convergence criteria were 10^{-6} Hartree and 10^{-3} Hartree Bohr^{-1}. Vibrational frequencies have been calculated using the harmonic approximation and analytical second derivatives for systems without continuum solvation, and numerical (central) second derivatives for systems with continuum solvation.[58–60] In the larger Ge clusters only displacements of the atoms corresponding to the ORR species and the directly attached GeH group have been considered. Due to the computational demand all other atoms were not displaced. A test calculation has shown that coupling with the vibrational modes of the water molecules is small and can be neglected for the bands of interest. Frequencies shift by ≤ 3 cm^{-1}. For better comparison to experimental frequencies the calculated values were scaled by 0.9691.[61]

Solvent effects were treated applying four different approaches:

(1) Neglecting solvent effects by simply calculating the molecules or clusters in a vacuum.

(2) Using the conductor-like screening model COSMO,[62] with a static dielectric constant $\varepsilon_r = 78.36$ and a refractive index $n = 1.333$ corresponding to water at 25 °C. This approach includes the polarisation effects due to the dielectric shielding of the electrolyte, however, neglects hydrogen bonds.

(3) Including explicit water molecules in the first solvation shell in order to include the effects of hydrogen bonds. For this purpose, a cluster of the solute and water molecules complexing each OH-group and lone pair is constructed. To secure a bulk-like isotropic solvation with a tetrahedral coordination of the solute oxygen(s) and nearly linear hydrogen bonds, the O_{water}–O_{solute}–O_{water} and O_{water}–O_{solute}–O_{solute} angles have been constrained to $\sim109°$. In the solvent shell of ClO_4^- and $HClO_4$, the water oxygen has been constrained to be collinear with the respective Cl–O bond.

(4) The solute–water complexes described in (3) were calculated with the COSMO conductor-like screening model to include the polarisation effects by the dielectric shielding on the hydrogen-bonded structures.

It should be noted that representing the dynamic and fluctuating water structure around a solute by a single partially optimized configuration is a crude approximation. Nevertheless it should represent the main trends in the vibrational modes due to aqueous solvation of solutes and adsorbed species.

For each of these solvation models the structures were optimized and vibrational frequencies were calculated as described above.

3 Results

3.1 Electrochemistry and ATR-IR spectroscopy

The CV in Fig. 1 in Ar closely resembles those reported under similar conditions.[38,40,41] An anodic peak at +0.1 V is attributed to the formation of a surface oxide.[38,40,41] At −0.3 V, a cathodic
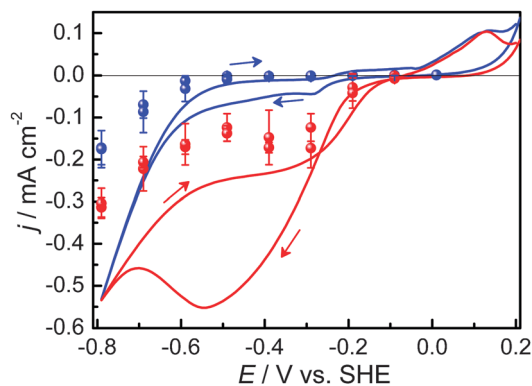

Fig. 1 Lines: CV (50 mV s^{-1}) of n-Ge(100) in O$_2$ (——) and Ar (——) saturated 0.1 M HClO$_4$. Arrows indicate the scan direction, the horizontal line (—) indicates current density $j = 0$. Symbols: average j during ATR-IR experiments in O$_2$ (●) and Ar (●).

Paper

PCCP

View Article Online

Open Access Article. Published on 04 mis Genver 2013. Downloaded on 21/06/2025 08:22:05.
This article is licensed under a Creative Commons Attribution-NonCommercial 3.0 Unported Licence.

current peak is observed, attributed to the onset of the change in surface termination from Ge–OH to Ge–H.[39,40] The surface transition has been proposed to be related to the onset of the ORR,[38,39] as it involves a radical surface state.[40,42,43] The H$_2$ evolution reaction (HER) dominates below −0.6 V.[38–40] In O$_2$ saturated solution, substantially increased currents are observed in the range −0.3 to −0.7 V in addition to surface oxidation at +0.1 V, and HER at potentials below −0.7 V.

Fig. 2 shows a series of ATR-IR spectra recorded using p-polarisation during the ORR on Ge(100) in the range of 1500 to 900 cm^{-1}. In the presence of O$_2$, three vibrational bands are observed, centered at 1030 cm^{-1}, 1210 cm^{-1}, and 1385 cm^{-1}. Another band at 1105 cm^{-1} is visible only as a shoulder in few spectra. This band is assigned to the antisymmetric Cl–O stretching mode of ClO$_4^-$ in solution (Table S1 and Fig. S3, ESI†).[63–65] In Ar, no bands are observed. The residual absorbance from bulk ClO$_4^-$ was subtracted from the spectra.

Using the procedures outlined in Section 2.2.1, the orientation of the TDMs of the vibrational modes observed has been determined. The orientations obtained are $(10 \pm 5)°$ for the mode at 1030 cm^{-1}, $(28 \pm 10)°$ for the mode at 1210 cm^{-1}, and $(35 \pm 10)°$ for the mode at 1385 cm^{-1}.
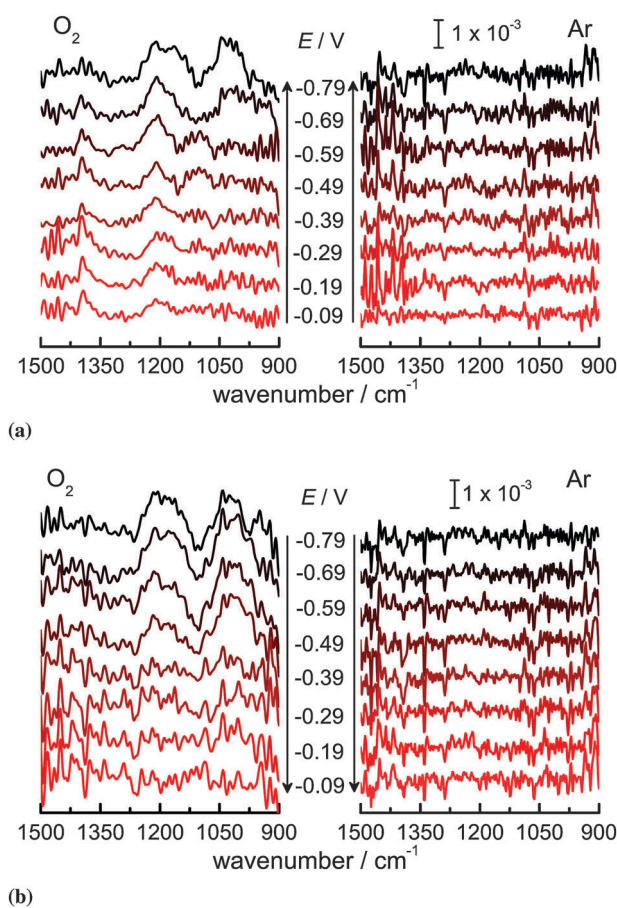

Fig. 2 ATR-IR absorbance spectra (p-polarisation) in O$_2$ and Ar saturated 0.1 M HClO$_4$ on Ge(100) in the direction of (a) more negative and (b) less negative potential.

3.2 DFT calculations

In order to arrive at a substantiated interpretation of the spectroelectrochemical experiments, a systematic study of possible ORR intermediates in solution and on the Ge(100) surface was carried out using DFT calculations. Solution species were derived from oxygen by adding electrons and protons in an alternating sequence until the O–O bond breaks after transfer of the third electron. The surface-bound species were constructed based on the experimental observation of a well-defined upright orientation of the TDMs, as reported in Section 3.1. This observation points to a covalent bond to the Ge surface, as will be discussed in Section 4.1. The clusters representing the germanium surface are cut from an ideal Ge(100) surface and all dangling bonds are saturated by hydrogen. A fully reduced surface covered with GeH$_2$ groups is assumed. Test calculations with models including ≻Ge(–H)–Ge(–H)≺ surface-dimers, which may result from a surface reconstruction, gave similar frequencies, however, require substantially higher computational resources due to the larger model structures. Here only the structures and vibrational modes relevant for this work are analyzed.

3.2.1 Vibrational frequencies of species in solution. Table 1 summarizes the vibrational frequencies calculated for various ORR related solution species applying the four different approaches to treat solvent effects. Calculated frequencies of H$_2$O, H$_2$O$_2$, HOO$^-$, HOO$^•$, O$_2^{•-}$, O$_2$, ClO$_4^-$ and HClO$_4$ are included, as well as experimental data from the literature and this work for comparison. Note that experimental data for gas phase species should only be compared to calculated frequencies of non-solvated molecules, while experimental data for aqueous solution should be compared to frequencies calculated for solvated molecules. The structures of the explicitly solvated molecules are shown in Fig. 3.

Solvation in water typically has a very significant effect on the vibrational frequencies. The experimental frequencies are shifted by ≈ 400 cm^{-1} to lower wavenumbers for the H$_2$O stretching modes ν(O–H) and shifted by 44 cm^{-1} to higher wavenumbers for the bending mode δ(H–O–H) due to solvation. The apparently small difference between the experimental gas phase and solution frequencies for the bending mode of H$_2$O$_2$ is due to the fact that there are actually two bending modes for H$_2$O$_2$. In the Raman experiment the symmetric mode is observed, while in the IR experiment the asymmetric mode is mainly contributing. According to the calculations (Table 1), these modes differ by more than 100 cm^{-1} and shift by 140 and 87 cm^{-1}, respectively, upon solvation.

Comparing the frequencies calculated with the four different solvation models shows that only the combination of explicit water molecules in the first hydration shell with the continuum solvation model COSMO properly reproduces the solvation effects. The continuum solvation model alone, as well as the explicit first solvation shell without COSMO, is clearly insufficient. Overall, the agreement of the B3-LYP/def2-TZVP scaled frequencies with the available experimental data is quite good. The root-mean-square deviation is 35 cm^{-1}. The largest deviations are +60 and −77 cm^{-1}.

5774 | *Phys. Chem. Chem. Phys.*, 2013, **15**, 5771–5781

This journal is © the Owner Societies 2013

Table 1 Vibrational frequencies, in cm^{-1}, of species in solution calculated with B3-LYP/def2-TZVP using the indicated solvation models and experimental reference data. For illustrations see Fig. 3

Species	Solvation model	Wavenumbers		
		ν(O–H)	δ(X–O–H)[a]	ν(O–O)
H_2O	None	3768/3667	1566	
	COSMO	3732/3647	1577	
	+4H_2O	3521/3450	1626	
	+4H_2O + COSMO	3381/3321	1626	
IR[66]	Gas phase	3756/3657	1595	
ATR-IR[67]	Liquid water	3351/3261	1639	
H_2O_2	None	3627/3626	1394[b]/1272	919[b]
	COSMO	3603/3598	1371[b]/1322	923[b]
	+6H_2O	3243/3203	1536[b]/1345	888[b]
	+6H_2O + COSMO	3089/3033	1534[b]/1359	936[b]
Raman[68]	Vapour	3607	1394	864
IR-ellipsometry[c]	30% H_2O_2		1380	
HOO^-	None	3624	1067	752
	COSMO	3644	1184	832
	+6H_2O	3548	1288	913
	+6H_2O + COSMO	3317	1364	901
IR-ellipsometry[c]	30% H_2O_2 + NaOH		1310	
$HOO^\bullet$	None	3458	1385	1126
	COSMO	3459	1407	1158
	+6H_2O	2817	1503	1214
	+6H_2O + COSMO	2492	1501	1196
UV-PES[69]	Vacuum			1125
$O_2^{\bullet-}$	None			1142[b]
	COSMO			1168[b]
	+6H_2O			1184[b]
	+6H_2O + COSMO			1183[b]
UV-PES[70]	He gas discharge			1090 ± 20
O_2	None			1583[b]
Raman[71]	Gas			1556

Species	Solvation	Wavenumbers		
		ν(O–H)	δ(Cl–O–H)	ν(Cl–O)
ClO_4^-	None			1070/890[b]
	COSMO			1069/897[b]
	+4H_2O			1083/915[b]
	+4H_2O + COSMO			1075/914[b]
ATR-IR[c]	0.1 M $HClO_4$			1105
Raman[65]	Dilute $HClO_4$			1113/934
$HClO_4$	None	3578	1284	1217/1167/1010/689
	COSMO	3522	1272	1200/1176/1007/703
	+6H_2O	2734	1366	1213/1213/1013/734
	+6H_2O + COSMO	1629	1417	1189/1177/962/780
Raman[65]	$HClO_4$			1220/1039/757

[a] X = H for H_2O, X = O elsewhere. [b] IR-inactive or almost IR-inactive. [c] This work.

3.2.2 Vibrational frequencies and orientation of intermediates at the Ge(100)/water interface. Binding motifs relevant for the observed vibrational modes have been identified with DFT calculation of clusters consisting of 3 Ge atoms. These results are listed in detail in the ESI.† Relevant species with vibrational modes in the range of interest have been used as starting point for calculations on $Ge_{13}H_{28}$ clusters that represent the space available at the fully hydrogenated Ge(100) surface (Fig. 4(a)). One of the two inward-pointing H-atoms at the central GeH_2

groups was substituted by the ORR intermediates. All O–H groups and lone pairs were coordinated by H-bonding water molecules as described for the solution species and solvent polarisation was accounted for using COSMO. The optimized structures are shown in Fig. 4 and the frequencies are summarized in Table 2.

4 Discussion

4.1 Discussion of the spectral interpretation of ATR-IR spectra during ORR

4.1.1 Peak at 1210 cm^{-1}. The major experimentally observed peak is centred at 1210 cm^{-1}. The DFT calculations (Tables 1 and 2, Table S2, ESI†) show three potential ORR intermediates with frequencies around the experimentally observed 1210 cm^{-1}: the OO stretching modes of $O_2^{\bullet-}$, $HOO^\bullet$, and a surface-bound superoxide $Ge–OO^\bullet$. Similar electrochemical ATR-IR experiments as above were performed in ^2H_2O-based electrolytes to check for frequency shifts with hydrogen–deuterium exchange. However, in ^2H_2O, the region around 1210 cm^{-1} cannot be easily analysed experimentally due to strong absorption from the bending mode of ^2H_2O. No shifted peaks were found in these experiments. While these observations present already indirect evidence for the assignment of the peak at 1210 cm^{-1} to an O–O stretching mode, direct evidence is the observation of an isotope shift when using $^{18}O_2$. For such experiments, the electrolyte was initially saturated with Ar, which was later replaced by $^{18}O_2$. Subsequently, electrolyte was pumped into the spectroelectrochemical cell. The spectrum in $^{18}O_2$ at −0.59 V referenced against the spectrum in Ar shows a shift of the peak to lower wavenumbers by 22 cm^{-1} (Fig. 5). Therefore, the O–O bond from the oxygen in the ORR must be a strong contributor to the vibrational mode causing the absorption. This experiment proves the assignment of the peak as the O–O stretching mode of an ORR intermediate – a superoxide according to the frequency. However, distinguishing between $O_2^{\bullet-}$, $HOO^\bullet$ and $Ge–OO^\bullet$ only on the basis of the small differences in the calculated frequencies would be ambiguous.

This peak cannot originate from an OOH bending mode. In alkaline H_2O_2, the bending mode of HOO^- is clearly observed at 1310 cm^{-1}, and comparison to H_2O_2, where no peak is observed at 1310 cm^{-1}, supports the assignment as bending mode of the HOO^- anion (Fig. S2, ESI†). The vicinity of the surface is not likely to shift the mode by more than a few cm^{-1}. From the expected modes of ORR intermediates, only the O–O stretching modes of superoxo-species are therefore in the spectral region where an absorption is observed experimentally.

From the dichroic ratio, a tilt angle $\theta \sim (28 \pm 10)°$ with respect to the surface normal has been determined for the TDM of the band at 1210 cm^{-1}, independent of the applied potential. The well-defined orientation of the TDM observed experimentally indicates that the vibrational mode at 1210 cm^{-1} is predominantly due to an intermediate covalently bound to the surface.

In the DFT calculations, the solvated model cluster for the surface-bound superoxide radical, $Ge_{13}H_{27}$-$OO^\bullet$·3H_2O (Fig. 4(e)), also has a very upright O–O bond (tilt angle 18°).
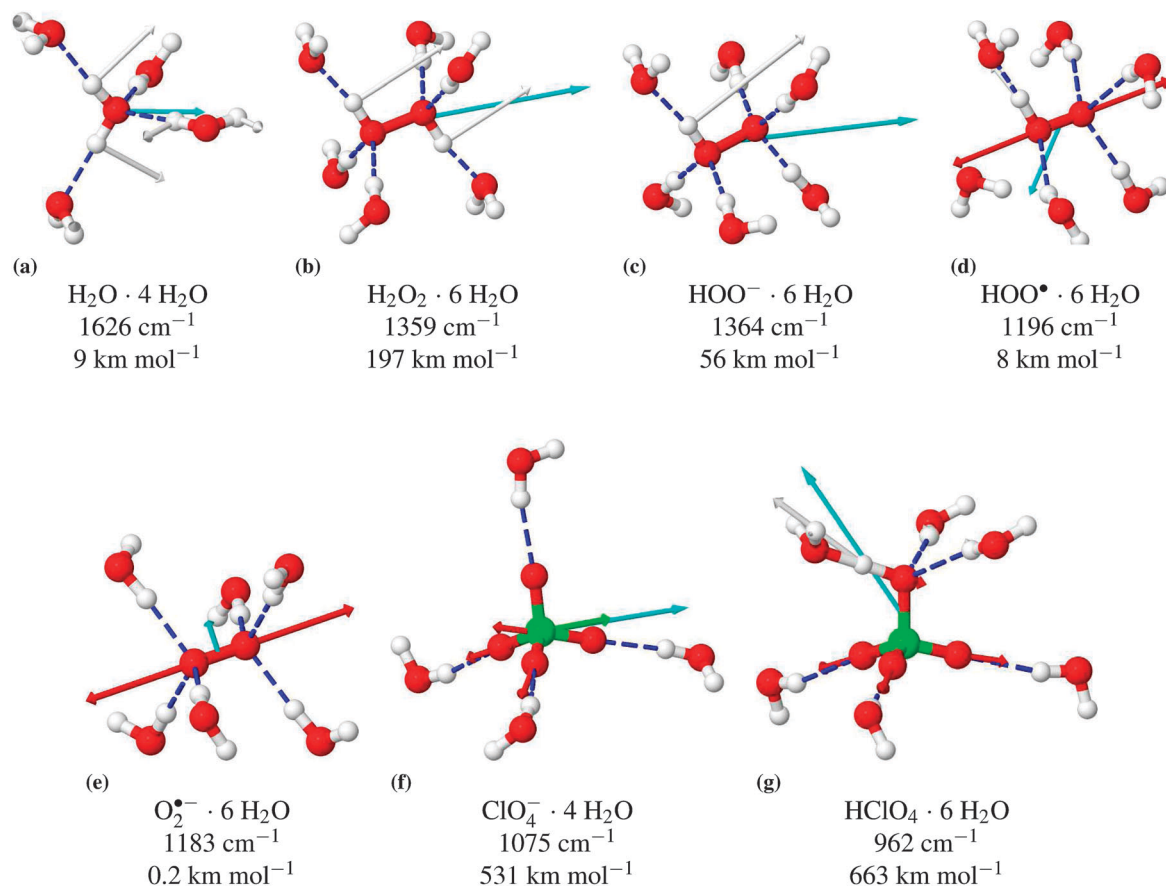
Fig. 3 Structures and selected vibrational modes, including absorption coefficient, of the explicitly solvated molecules calculated with COSMO. Overview of vibrational frequencies at different solvation models, see Table 1. Hydrogen bonds are depicted as — — —. The motion of the atoms during the respective vibrational modes are indicated as arrows in the color of the respective atom. The direction and magnitude of the TDM are shown as arrows in cyan (→).

The stretching mode ν(O–O) at 1159 cm^{-1} is in good agreement with the experimental value of 1210 cm^{-1}. The tilt angle of the calculated TDM of 40° is in reasonable agreement with the experimental tilt angle of (28 ± 10)°.

4.1.2 Peak at 1385 cm^{-1}. The band at 1385 cm^{-1} is assigned to the O–O–H bending mode of a peroxide, which could originate either from H$_2$O$_2$, from HOO$^-$, or from surface-bound Ge–OOH according to the DFT calculations (Tables 1, 2 and Table S2, ESI†). In control experiments, the bending mode of H$_2$O$_2$ is observed at 1380 cm^{-1}, while the OOH$^-$ bending mode is found at 1310 cm^{-1} (Fig. S2(b), ESI†), which rules out OOH$^-$ as the origin of the 1385 cm^{-1} band.

Comparing the peak frequency of the OOH bending mode in H$_2$O$_2$ to the one observed in ORR experiments at 1385 cm^{-1} gives agreement within 5 cm^{-1}. However, the mode on the Ge surface observed during ORR has a full width at half maximum of 20 cm^{-1}, while in H$_2$O$_2$ it is much wider (FWHM 150 cm^{-1}). Contributing to the width for the absorption in the bulk spectra is likely the fact that (i) each molecule has two normal modes around 1400 cm^{-1}, and (ii) these modes are slightly shifted for different conformations and solvation states of H$_2$O$_2$.

For this absorption, an orientation of $\theta \sim$ (35 ± 10)° has been determined at potentials where the peak is clearly observed in the spectra, *i.e.* at the initial three potentials.

The observed very narrow peak in the ORR experiments, together with the dichroism observed, leads to the assignment of this mode to surface-bound peroxide, as opposed to bulk H$_2$O$_2$.

The surface model cluster with a solvated Ge-bound peroxide group, Ge$_{13}$H$_{27}$-OOH·3H$_2$O (Fig. 4(c)), has a fairly upright O–O bond tilted 15° with respect to the surface normal. The neighbouring GeH$_2$ groups and the space required by the solvation shell enforce this upright orientation (Fig. 4(c)). The solvated cluster shows a bending mode δ(O–O–H) at 1427 cm^{-1} in good agreement with the observed frequency at 1385 cm^{-1}. The corresponding TDM is tilted by 17°. This is in acceptable agreement with the experimental tilt angle of (35 ± 10)°. It should be noted that only one representative structure has been calculated. More accurate simulations would have to sample thermal motion of the functional group and fluctuations in the solvation shell.

4.1.3 Peak at 1030 cm^{-1}. The peak centred around 1030 cm^{-1} is also ORR-related as it does not appear in the control experiment under Ar. However, the frequency is unusual for an O–O stretching vibration lying between the ranges observed for superoxide and peroxide species.[22,30] Calculations of model compounds corresponding to superoxides or peroxides in different geometrical arrangements on Ge(100) and different binding sites fail to show
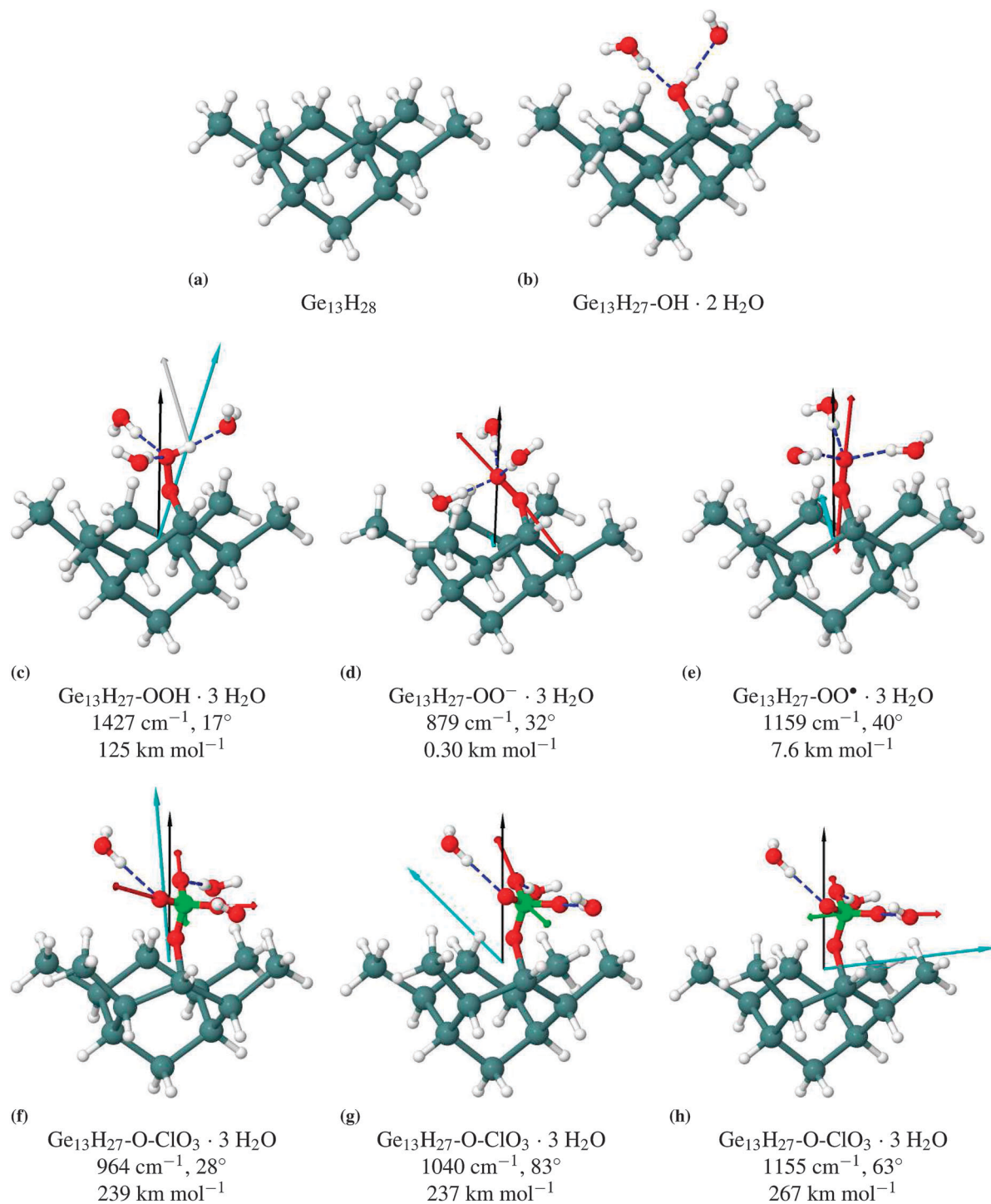
(a) $Ge_{13}H_{28}$

(b) $Ge_{13}H_{27}\text{-OH} \cdot 2\,H_2O$

(c) $Ge_{13}H_{27}\text{-OOH} \cdot 3\,H_2O$
1427 cm^{-1}, 17°
125 km mol^{-1}

(d) $Ge_{13}H_{27}\text{-OO}^- \cdot 3\,H_2O$
879 cm^{-1}, 32°
0.30 km mol^{-1}

(e) $Ge_{13}H_{27}\text{-OO}^{\bullet} \cdot 3\,H_2O$
1159 cm^{-1}, 40°
7.6 km mol^{-1}

(f) $Ge_{13}H_{27}\text{-O-ClO}_3 \cdot 3\,H_2O$
964 cm^{-1}, 28°
239 km mol^{-1}

(g) $Ge_{13}H_{27}\text{-O-ClO}_3 \cdot 3\,H_2O$
1040 cm^{-1}, 83°
237 km mol^{-1}

(h) $Ge_{13}H_{27}\text{-O-ClO}_3 \cdot 3\,H_2O$
1155 cm^{-1}, 63°
267 km mol^{-1}

Fig. 4 Structures of the explicitly solvated surface clusters optimized with COSMO. Important vibrational modes are represented by their atomic velocity vectors. The TDM is indicated in cyan (→) and the surface normal in black (→). Together with the chemical formula of the cluster, the wavenumber, tilt angle of the TDM and the absorption coefficients are given below with the respective structure. An overview of the relevant vibrational frequencies is given in Table 2.

frequencies in this range (Table 2 and Table S2, ESI†). Bands around 1040 cm^{-1} have been reported for ClO_4^- and $HClO_4$.[21,65,72] In particular, a symmetric Cl–O stretching mode at 1039 cm^{-1} is reported for undissociated $HClO_4$,[65] which, however, is unlikely to be present in the diluted acid used here. This characteristic vibrational mode persists if ClO_4^- is bound

via an O-atom to a Ge surface site (Fig. 4(f–h)). Calculations for the Ge–O–ClO_3 group show one symmetric (964 cm^{-1}) and two asymmetric (1040 and 1155 cm^{-1}) Cl–O stretching modes.

Analysis of the dichroic ratio shows that the TDM belonging to this mode is oriented nearly perpendicular to the surface, *i.e.* almost coinciding with the surface normal, $\theta \sim (10 \pm 5)°$.

Table 2 Selected vibrational frequencies of hydrated model clusters for surface-bound ORR intermediates at the Ge(100)/water interface, in cm^{-1}, calculated with B3-LYP/def2-TZVP, COSMO. The second column indicates the part of Fig. 4 displaying the respective structure

Species		Wavenumbers				
		ν(O–H)	ν(Ge–H)	δ(O–O–H)	ν(O–O)	ν(Ge–O)
$Ge_{13}H_{28}$	(a)		2044/2033/2019/2018			
$Ge_{13}H_{27}$-OH·$2H_2O$	(b)	3359	1971	1106		635
$Ge_{13}H_{27}$-OOH·$3H_2O$	(c)	3145	2032	1427	911	548
$Ge_{13}H_{27}$-OO$^-$·$3H_2O$	(d)		1985		879	607
$Ge_{13}H_{27}$-OO$^\bullet$·$3H_2O$	(e)		2041		1158	471
$Ge_{13}H_{27}$-O-ClO$_3$·$3H_2O$	(f–h)		2035	1155/1040/964/768^a		623

^{a} ν(Cl–O).
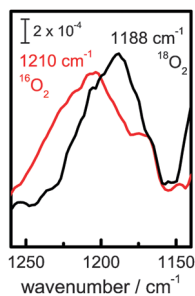
Fig. 5 Isotope shift of mode at 1210 cm^{-1} when working in an $^{18}O_2$ containing electrolyte at −0.59 V.

Fig. 6 Potential dependence of A_{iso} of the O–O stretching mode at 1210 cm^{-1} (in the direction of ○ negative and ◆ positive potentials) and ORR current densities j_{ORR} (in the direction of ○ negative and ◆ positive potentials). Inset: comparison of j_{ORR} (as in the main figure) with the experimental j_{O_2} (in the direction of ○ negative and ◆ positive potentials).

The DFT calculations also show the surface-bound perchlorate to have a fairly upright standing conformation in the solvated surface cluster, $Ge_{13}H_{27}$-O-ClO$_3$·$3H_2O$ (Fig. 4(f–h)). The Cl–O bond of the Ge-bound O-atom has a tilt angle of 26° with respect to the surface normal. The calculated frequency of the symmetric stretching mode ν_{sym}(Cl–O) of 964 cm^{-1} is lower than the experimental frequency of 1030 cm^{-1}. However, this deviation is systematic as it was also observed for the ν(Cl–O) frequencies in HClO$_4$. The corresponding TDM has a tilt angle of 28° in agreement with the very upright orientation of $(10 \pm 5)°$ determined in the ATR experiment. This strong orientation confirms the assignment to the symmetric ClO$_3$ stretching mode of the surface-bound perchlorate. The two asymmetric stretching modes ν_{as}(Cl–O) at 1040 cm^{-1} and 1155 cm^{-1} have TDMs oriented nearly parallel to the surface with tilt angles of 83° and 63°. Both calculated frequencies are probably underestimated due to a systematic error and at least the one at higher frequency may contribute absorbance in the region of the superoxide species ($\approx$1200 cm^{-1}). The fourth mode at 768 cm^{-1} belongs to the O-atom which is bound to the Ge surface, and is outside the range of interest.

4.2 Mechanism of the ORR on Ge(100)

The integrated absorbances in p- and s-polarisation of the mode centred at 1210 cm^{-1} have been transformed into an orientation-independent isotropic absorbance (A_{iso}), which is proportional to the surface coverage of the respective species. The resulting A_{iso} are shown in Fig. 6 in comparison with the pure ORR current densities ($j_{ORR} = j_{O_2} - j_{Ar}$), obtained as a difference between total measured current densities in O$_2$ (j_{O_2})

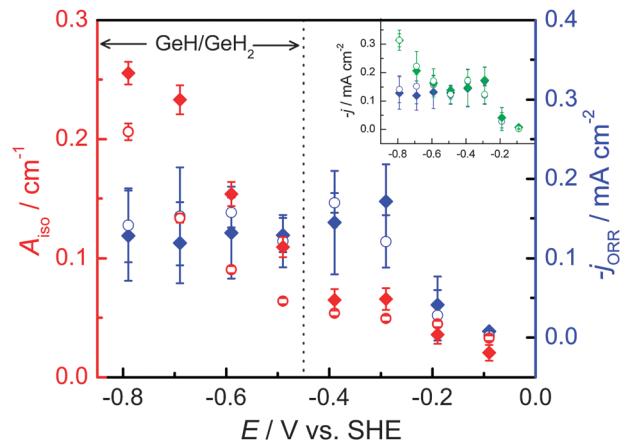and Ar (j_{Ar}). At −0.1 to −0.3 V, the increase in current follows the increase in absorbance, until a plateau is reached in both current and A_{iso} between −0.3 and −0.5 V. Consequently, there is a correlation of the net ORR reaction rate ($\propto j_{ORR}$) with the surface concentration of superoxide ($\propto A_{iso}$). Below −0.5 V the surface is fully H-terminated, as shown by the Ge–H stretching modes.[39,40] At the Ge–H terminated surface, A_{iso} increases at highly negative potential, as does j_{O_2} (see the inset), while j_{ORR} remains constant. The increase in j_{O_2} is related to the HER, while the increase in A_{iso} correlates with the appearance of the vibrational band at 1030 cm^{-1}. The increase in A_{iso} at the three most negative potentials (−0.59 to −0.79 V) is therefore caused by the presence of surface-bound perchlorate, which also contributes weakly to the peak at 1210 cm^{-1}.

The OOH bending mode is present initially, and decreases in absorbance at more negative potentials. Therefore, at the initial slightly negative potentials, the rate of peroxide formation exceeds its reduction rate. In the reverse scan, the absorbance of this band is on the level of the noise, which is attributed to changes in the surface structure during the experiment. While the absorption coefficient obtained from the DFT calculations of the OOH bending mode is higher than the absorption coefficient of the O–O stretching mode of
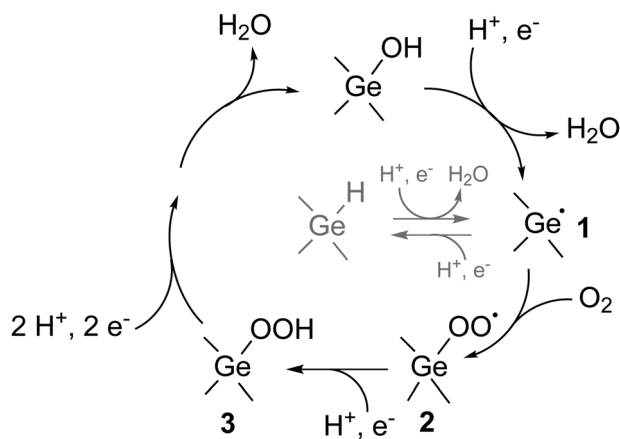
Fig. 7 Cycle with proposed mechanism for the ORR on Ge. Open bonds on the Ge atoms symbolize bonds to bulk Ge or other surface atoms. The radical species **1** has been proposed earlier,[38,42] species **2** and **3** are identified in this work. Models for these and the respective vibrational modes are shown in Fig. 4(e) (**2**) and Fig. 4(c) (**3**).

Table 3 Summary of the tilt angles θ of the TDMs with respect to the surface normal of the transient species observed during ORR, and in comparison with DFT calculations

Peak absorption	1210 cm^{-1}	1385 cm^{-1}	1030 cm^{-1}
Assignment	ν(O–O)	δ(O–O–H)	ν_{sym}(Cl–O)
Species	Ge–O$_2^{\bullet-}$	Ge–OOH	Ge–OClO$_3$
Exp. tilt angle θ	$(28 \pm 10)°$	$(35 \pm 10)°$	$(10 \pm 5)°$
Calc. θ (TDM)	40°	17°	28°
Calc. θ (bond)	21$°^a$	18$°^a$	26$°^b$

^{a} O–O bond. ^{b} Cl–O bond.

surface-bound superoxide by a factor of 20, its observed absorbance is considerably lower. To explain this observation, it should be noted that the absorbance is a function of the concentration at and near the Ge/electrolyte interface. The concentration of the surface-bound peroxide is therefore considerably lower than the concentration of surface-bound superoxide.

The absorbance of surface-bound perchlorate at 1030 cm^{-1} correlates with the HER current. This absorption is, however, not present in Ar, therefore is not related to the HER alone. This species may form in a side reaction of the ORR. However, it may also point to the active involvement of the electrolyte in the ORR.

The observation of a Ge-bound superoxide as an intermediate in the ORR suggests that the ORR starts by the combination of an O$_2$ molecule with a surface radical. Such surface radicals have been discussed as intermediates in the transformation from the OH- to the H-terminated surface, in the HER and as sites for the reduction of H$_2$O$_2$.[38,40,43] Further reduction of the Ge–O$_2^{\bullet-}$ and proton transfer leads to the second intermediate, Ge–OOH, observed in this work at slightly negative potentials. An alternative mechanism starting with the insertion of O$_2$ into a Ge–H bond would directly lead to Ge–OOH bypassing the Ge–OO$^{\bullet}$, which is inconsistent with the observations of this work. Based on the Ge-bound intermediates identified in the electrochemical ATR-IR experiments and on the mechanisms for the change in surface termination and HER,[38,40] we propose the catalytic cycle as shown in Fig. 7. This mechanism includes the surface radical as a common surface active site in both ORR and HER, thus providing a coupling mechanism between the two reactions.

5 Conclusion

A summary of the vibrational modes observed, their assignment based on the evidence presented here and the TDM orientation is given in Table 3. In conclusion, the electrochemical ORR on Ge(100) in aqueous HClO$_4$ proceeds *via* a stepwise mechanism

transferring one electron at a time. The active radical species is generated initially by reduction of the surface, which subsequently reacts with O$_2$. The first electrochemical reduction step therefore happens not at the molecule to be activated, but at the surface and is followed by a chemical reduction of oxygen. The presence of large concentration of such reduced surface sites may prove crucial for the activity of a surface towards the ORR. A surface-bound superoxide (Ge–OO$^{\bullet}$) with a TDM at a tilt angle of $(28 \pm 10)°$ was detected as the main intermediate. The distinctly upright orientation implies that the superoxide is not bridging between different Ge atoms, not bound side-on to a single Ge-atom, and not dissolved. Rather, it is close to what is expected for the Pauling model.[2] The surface concentration of superoxide increases at strongly negative potential until the surface is fully H-terminated. Especially before full H-termination, the surface-bound peroxide (Ge–OOH) with a similar orientation to the superoxide is generated at a higher rate than the rate with which it is consumed. Though this work does not address the role of structural defects, detailed experimental information on the ORR mechanism as presented here may help in future knowledge-based theory-guided design of improved catalysts and corrosion inhibition systems. Application of the methodology developed here to relevant oxides is currently under investigation.

References

1 J. P. Hoare, *The Electrochemistry of Oxygen*, Interscience, New York, 1968.
2 K. Kinoshita, *Electrochemical Oxygen Technology*, Wiley, New York, 1992, vol. 1117.
3 F. Cheng and J. Chen, *Chem. Soc. Rev.*, 2012, **41**, 2172–2192.
4 I. E. L. Stephens, A. S. Bondarenko, U. Gronbjerg, J. Rossmeisl and I. Chorkendorff, *Energy Environ. Sci.*, 2012, **5**, 6744–6762.
5 Y. Feng, A. Gago, L. Timperman and N. Alonso-Vante, *Electrochim. Acta*, 2011, **56**, 1009–1022.

6 F. Jaouen, E. Proietti, M. Lefevre, R. Chenitz, J.-P. Dodelet, G. Wu, H. T. Chung, C. M. Johnston and P. Zelenay, *Energy Environ. Sci.*, 2011, **4**, 114–130.

7 N. Ramaswamy and S. Mukerjee, *Adv. Phys. Chem.*, 2012, **2012**, 491604.

8 J. D. Wiggins-Camacho and K. J. Stevenson, *J. Phys. Chem. C*, 2011, **115**, 20002–20010.

9 E. M. Erickson, M. S. Thorum, R. Vasić, N. S. Marinković, A. I. Frenkel, A. A. Gewirth and R. G. Nuzzo, *J. Am. Chem. Soc.*, 2012, **134**, 197–200.

10 J.-M. Noël, A. Latus, C. Lagrost, E. Volanschi and P. Hapiot, *J. Am. Chem. Soc.*, 2012, **134**, 2835–2841.

11 N. Lopez, D. J. Graham, R. McGuire, G. E. Alliger, Y. Shao-Horn, C. C. Cummins and D. G. Nocera, *Science*, 2012, **335**, 450–453.

12 N. Anastasijevic, V. Vesovic and R. R. Adzic, *J. Electroanal. Chem.*, 1987, **229**, 305–316.

13 J. K. Nørskov, J. Rossmeisl, A. Logadottir, L. Lindqvist, J. R. Kitchin, T. Bligaard and H. Jónsson, *J. Phys. Chem. B*, 2004, **108**, 17886–17892.

14 Y. Wang and P. B. Balbuena, *J. Phys. Chem. B*, 2005, **109**, 14896–14907.

15 T. Jacob and W. A. Goddard, *ChemPhysChem*, 2006, **7**, 992–1005.

16 S. Walch, A. Dhanda, M. Aryanpour and H. Pitsch, *J. Phys. Chem. C*, 2008, **112**, 8464–8475.

17 J. S. Spendelow and A. Wieckowski, *Phys. Chem. Chem. Phys.*, 2007, **9**, 2654–2675.

18 A. A. Gewirth and M. S. Thorum, *Inorg. Chem.*, 2010, **49**, 3557–3566.

19 H. S. Wroblowa, Y.-C. Pan and G. Razumney, *J. Electroanal. Chem. Interfacial Electrochem.*, 1976, **69**, 195–201.

20 B. B. Blizanac, A. C. Lucas, E. M. Gallagher, M. Arenz, N. P. Ross and M. N. Markovic, *J. Phys. Chem. B*, 2004, **108**, 625–634.

21 X. Li and A. A. Gewirth, *J. Am. Chem. Soc.*, 2005, **127**, 5252.

22 T. Itoh, T. Maeda and A. Kasuya, *Faraday Discuss.*, 2006, **132**, 95–109.

23 M. Shao, P. Liu and R. R. Adzic, *J. Am. Chem. Soc.*, 2006, **128**, 7408–7409.

24 J. Brooker, P. A. Christensen, A. Hamnett and R. He, *Faraday Discuss.*, 1992, **94**, 339–360.

25 T. Itoh, K. Abe, K. Dokko, M. Mohamedi, I. Uchida and A. Kasuya, *J. Electrochem. Soc.*, 2004, **151**, A2042–A2046.

26 M. H. Shao and R. R. Adzic, *J. Phys. Chem. B*, 2005, **109**, 16563–16566.

27 J. Kim and A. A. Gewirth, *J. Phys. Chem. B*, 2006, **110**, 2565–2571.

28 Y. Ayato, K. Kunimatsu, M. Osawa and T. Okadaa, *J. Electrochem. Soc.*, 2006, **153**, A203–A209.

29 K. Kunimatsu, T. Yoda, D. A. Tryk, H. Uchida and M. Watanabe, *Phys. Chem. Chem. Phys.*, 2010, **12**, 621–629.

30 C. Pettenkofer, I. Pockrand and A. Otto, *Surf. Sci.*, 1983, **135**, 52–64.

31 P. Vassilev and M. T. M. Koper, *J. Phys. Chem. C*, 2007, **111**, 2607–2613.

32 J. A. Keith, G. Jerkiewicz and T. Jacob, *ChemPhysChem*, 2010, **11**, 779–2794.

33 J. B. MacNaughton, L.-A. Naslund, T. Anniyev, H. Ogasawara and A. Nilsson, *Phys. Chem. Chem. Phys.*, 2010, **12**, 5712–5716.

34 A. Gonchar, T. Risse, H.-J. Freund, L. Giordano, C. Di Valentin and G. Pacchioni, *Angew. Chem., Int. Ed.*, 2011, **50**, 2635–2638.

35 K. Bohnenkamp and H. Engell, *Z. Elektrochem.*, 1957, **61**, 1184–1196.

36 A. W. Hassel and J. W. Schultze, Passivity of Metals, Alloys, and Semiconductors, in *Encyclopedia of Electrochemistry*, Volume 4, Corrosion and Oxide Films, ed. M. Stratmann and G. S. Frankel, Wiley-VCH, Weinheim, 2003, pp. 216–270.

37 K. Gong, F. Du, Z. Xia, M. Durstock and L. Dai, *Science*, 2009, **323**, 760–764.

38 R. Memming and G. Neumann, *J. Electroanal. Chem.*, 1969, **21**, 295–305.

39 F. Maroun, F. Ozanam and J.-N. Chazalviel, *J. Phys. Chem. B*, 1999, **103**, 5280–5288.

40 J.-N. Chazalviel, A. Belaïdi, M. Safi, F. Maroun, B. Erne and F. Ozanam, *Electrochim. Acta*, 2000, **45**, 3205–3211.

41 F. Maroun, J.-N. Chazalviel, F. Ozanam and D. Lincot, *J. Electroanal. Chem.*, 2003, **549**, 161–163.

42 A. Maurer, W. Mindt and H. Gerischer, *Surf. Sci.*, 1966, **4**, 431–439.

43 H. Gerischer and W. Mindt, *Surf. Sci.*, 1966, **4**, 440–451.

44 W. Brattain and C. Garrett, *Bell Syst. Tech. J.*, 1955, **34**, 129–176.

45 A. Erbe, http://home.arcor.de/aerbe/en/prog/spectraltools.html, 2012.

46 E. Goormaghtigh, V. Raussens and J.-M. Ruysschaert, *Biochim. Biophys. Acta, Biomembr.*, 1999, **1422**, 105–185.

47 N. Harrick, *Internal Reflection Spectroscopy*, Harrick Scientific, 1987.

48 A. Erbe, R. J. Bushby, S. D. Evans and L. J. C. Jeuken, *J. Phys. Chem. B*, 2007, **111**, 3515–3524.

49 G. Gonella, H.-L. Dai, H. C. Fry, M. J. Therien, V. Krishnan, A. Tronin and J. K. Blasie, *J. Am. Chem. Soc.*, 2010, **132**, 9693–9700.

50 P. Wenzl, M. Fringeli, J. Goette and U. P. Fringeli, *Langmuir*, 1994, **10**, 4253–4264.

51 TURBOMOLE V6.2 2010, a development of University of Karlsruhe and Forschungszentrum Karlsruhe GmbH, 1989–2007, TURBOMOLE GmbH, since 2007; available from http://www.turbomole.com.

52 A. D. Becke, *Phys. Rev. A: At., Mol., Opt. Phys.*, 1988, **38**, 3098–3100.

53 C. Lee, W. Yang and R. G. Parr, *Phys. Rev. B: Condens. Matter Mater. Phys.*, 1988, **37**, 785–789.

54 A. D. Becke, *J. Chem. Phys.*, 1993, **98**, 5648–5652.

55 F. Weigend and R. Ahlrichs, *Phys. Chem. Chem. Phys.*, 2005, **7**, 3297–3305.

56 F. Weigend, *Phys. Chem. Chem. Phys.*, 2006, **8**, 1057–1065.

57 F. Weigend, *Phys. Chem. Chem. Phys.*, 2002, **4**, 4285–4291.

58 P. Deglmann, F. Furche and R. Ahlrichs, *Chem. Phys. Lett.*, 2002, **362**, 511–518.

5780 | *Phys. Chem. Chem. Phys.*, 2013, **15**, 5771–5781

This journal is © the Owner Societies 2013
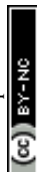
59 P. Deglmann and F. Furche, *J. Chem. Phys.*, 2002, **117**, 9535–9538.

60 A. Klamt, *J. Phys. Chem.*, 1996, **100**, 3349–3353.

61 P. Sinha, S. E. Boesch, C. Gu, R. A. Wheeler and A. K. Wilson, *J. Phys. Chem. A*, 2004, **108**, 9213–9217.

62 A. Klamt and G. Schuurmann, *J. Chem. Soc., Perkin Trans. 2*, 1993, 799–805.

63 L. Bencivenni, R. Caminiti, A. Feltrin, F. Ramondo and C. Sadun, *J. Mol. Struct. (THEOCHEM)*, 1992, **257**, 369–403.

64 A. Karelin, Z. Grigorovich and V. Rosolovskii, *Spectrochim. Acta, Part A*, 1975, **31**, 765–775.

65 C. I. Ratcliffe and D. E. Irish, *Can. J. Chem.*, 1984, **62**, 1134–1144.

66 T. Shimanouchi, *Tables of Molecular Vibrational Frequencies Consolidated Volume I*, National Bureau of Standards, Gaithersburg, 1972.

67 S. E. Lappi, B. Smith and S. Franzen, *Spectrochim. Acta, Part A*, 2004, **60**, 2611–2619.

68 P. A. Giguère and T. K. K. Srinivasan, *J. Raman Spectrosc.*, 1974, **2**, 125–132.

69 T. M. Ramond, S. J. Blanksby, S. Kato, V. M. Bierbaum, G. E. Davico, R. L. Schwartz, W. C. Lineberger and G. B. Ellison, *J. Phys. Chem. A*, 2002, **106**, 9641–9647.

70 K. M. Ervin, I. Anusiewicz, P. Skurski, J. Simons and W. C. Lineberger, *J. Phys. Chem. A*, 2003, **107**, 8521–8529.

71 A. Weber and E. A. McGinnis, *J. Mol. Spectrosc.*, 1960, **4**, 195–200.

72 X. Li and A. A. Gewirth, *J. Raman Spectrosc.*, 2005, **36**, 715–724.